Available online at www.sciencedirect.com
ScienceDirect
Planetary and Space Science 55 (2007) 1518–1529
Planetary and Space Science
www.elsevier.com/locate/pss

Development of an LENA instrument for planetary missions by numerical simulations

Yoichi Kazama[a,*,1], Stas Barabash[a], Martin Wieser[a], Kazushi Asamura[b], Peter Wurz[c]

[a]Swedish Institute of Space Physics, SE-981 28, Kiruna, Sweden
[b]Institute of Space and Astronautical Science, Japan Aerospace and Exploration Agency, Sagamihara, Kanagawa 229-8510, Japan
[c]University of Bern, CH-3012 Bern, Switzerland

Accepted 15 November 2006
Available online 1 March 2007

Abstract

Low-energy neutral atom (LENA) observations bring us important information on particle environments around celestial objects such as Mercury and the Moon. In this paper, we report on new development of an LENA instrument for planetary explorations. The instrument is light weight (2 kg), and capable of mass and energy discrimination with a large sensitivity. The performance of the instrument is investigated by numerical simulations. By using our new computer code, we calculated 3D particle trajectories including ionization, neutralization, surface scattering, and secondary electron creation. This enables us to obtain detailed performance characterization of LENA measurements. We also made trajectory tracing of photons entering the instrument to acquire photon rejection capability. This LENA instrument has been selected for both the Indian lunar exploration mission Chandrayaan-1 and European–Japanese Mercury exploration mission BepiColombo.

Keywords: Mercury; Moon; ENA; Bepi Colombo; Chandrayaan-1; Instrumentation

1. Introduction

Energetic neutral atoms (ENAs) are neutral particles created through high-energy collisions. In this section, ENAs at Mercury will be mentioned first, then we move to ENAs at the Moon.

Neutral particles play an important part in Mercury's particle environment as well as charged particles do, because charged and neutral particles are tightly coupled with each other; ions create ENAs, which can change into ions again. Processes of creating ENAs are: (1) sputtering of surface materials, (2) charge-exchange of energetic ions with exospheric gases, and (3) back-scattering of energetic particles precipitating toward the surface.

Solar-wind and magnetospheric ions can precipitate to Mercury's surface directly, and a large amount of low-energy neutral atoms (LENAs) are sputtered upward to form the exosphere around Mercury. According to the Thompson–Sigmund formula (Thompson, 1968), these LENAs have energies from 0 to 100 eV and more. In addition to the sputtering process, precipitating solar-wind ions are scattered back to space as neutrals. Although momentum loss occurs on scattering, back-scattered ENAs still keep high energies of 1 keV down to ~100 eV.

Hence, measuring LENAs coming from the surface gives us locations of precipitating energetic particles where LENAs 'shine'. Since a sputtered LENA originates from the surface, we can also 'see' species of the surface materials remotely by LENA measurement.

Solar-wind ions and magnetospheric ions can charge-exchange with gases in Mercury's exosphere, which also creates ENAs. Thus, ENA observation enables us to know the structure and dynamics of Mercury's magnetosphere which changes fast in time (e.g., Christon et al., 1979; Christon, 1987).

Some ENAs hit the surface and sputter the surface materials as LENAs, which are converted into ions again.

*Corresponding author. Tel.: +81 29 8684 213; fax: +81 29 868 5970.
E-mail address: kazama.yoichi@jaxa.jp (Y. Kazama).
[1]Now at Institute of Aerospace Technology, Japan Aerospace and Exploration Agency, Tsukuba, Ibaraki 305-8505, Japan.

0032-0633/$ - see front matter © 2007 Elsevier Ltd. All rights reserved.
doi:10.1016/j.pss.2006.11.027

This cyclic process makes charged and neutral particle environments coupled together. Therefore, ENA observation at Mercury is complementary to ion observation, and is important to achieve comprehensive understanding of Mercury's particle environment.

In the case of the Moon, the main processes of creating ENAs are sputtering and back-scattering; charge exchange rarely takes place because an exosphere does not exist (Wurz et al., 2007). The solar wind directly hits the lunar surface and sputters LENAs, or is scattered back into space as well as at Mercury.

Recently, local magnetic anomalies have been found on the lunar surface (Lin et al., 1998). At the anomalies, small magnetic fields exist and are expected to form 'mini magnetospheres'. The magnetic fields stop the solar wind from hitting the surface, which makes 'dark spots' in ENA images. Measurement of ENA at the Moon will provide information about these characteristic magnetic field anomalies.

The solar-wind sputters surface materials toward space in a similar way at Mercury. Accordingly, global remote sensing of surface elements can be also available at the Moon (Wurz et al., 2007). In addition, it is also noted that ENA measurements at the Moon are important in terms of space weathering to understand the evolution of planetary surfaces unprotected by an atmosphere.

The Swedish Institute of Space Physics (Institutet för rymdfysik; IRF) is now developing an LENA instrument in cooperation with Institute of Space and Astronautical Science (ISAS) in Japan, and University of Bern (UBe) in Switzerland. The instrument has been selected for the Indian Moon exploration mission Chandrayaan-1 (Bhardwaj et al., 2005), and the European–Japanese Mercury exploration mission BepiColombo. In this paper, we report in detail expected performances of the instrument by numerical simulations.

2. Design requirements

To meet the scientific purposes of ENA observation at Mercury and at the Moon, an ENA instrument needs (1) to be light weight because of mass limitation in planetary missions, (2) high sensitivity for tenuous/low-energy ENA detection, (3) mass discrimination for determining sources and surface elements, and (4) angular coverage and resolution for ENA mapping.

The strongest requirement is the mass limitation of the whole instrument for the above-mentioned missions, of 2 kg in total, and the other requirements have lower priority compared to the mass. Therefore, the most important point in developing the instrument is to seek the design that maximizes each performance with keeping capability for the scientific purposes. We have made repeated computer simulations, and have achieved the total weight of 2 kg of the whole instrument (sensor and electronics) which is capable of fulfilling the scientific aim.

According to Lukyanov et al. (2004), LENA fluxes at Mercury are estimated at $10^1 - 10^3/\mathrm{s\,cm^2\,sr\,eV}$ in the energy range of 10–100 eV. Assuming an LENA flux $j = 10^1/\mathrm{s\,cm^2\,sr\,eV}$ and one count per 100 s ($C/\Delta t = 1/100$), the overall energy-integrated sensitivity $G = (C/\Delta t)/j = 10^{-3}\,\mathrm{cm^2\,sr\,eV}$ should be achieved for LENA measurements.

For low-energy (~10 eV) ENA detection, the conventional thin-foil ionization method cannot be used because low-energy particles cannot pass through the foil. We employ specially developed surfaces to ionize ENAs (Wurz, 2000). This method has been well established by IRF and UBe in the ASPERA-3 and ASPERA-4 instruments (e.g., Barabash et al., 2004, 2007).

Since low count rates of ENAs, for example, 0.01 count/s as taken above, are expected, the instrument must have a good signal-to-noise ratio.

To reject noise, we use two techniques: (1) a wave-type structure with serrated walls to block photons, and (2) anti-coincidence detection to reject non-ENA signals.

UBe has developed an instrument with a wave-type structure in combination with serrated walls for the SOHO mission, which showed the photon rejection ratio of 2×10^{-8} (Hovestadt et al., 1995). Anti-coincidence technique is widely used in particle instruments, and IRF also has been well-experienced with this technique, e.g., neutral particle detector (NPD) of the ASPERA-3 instruments onboard Mars Express (Barabash et al., 2004).

3. Design of the instrument

Fig. 1 illustrates a cross-sectional view of the whole instrument in three dimensions. The coordinate system used through this study is also given. The instrument consists of the sensor and the electronics, and the circuit boards are placed on the right side of the instrument in the figure. The sensor has two parts of semicylinder-like shape, both of which are concentric and faced at $X = 0$.

Fig. 2 displays the cross-section of the model structure of the sensor part created in the simulation space. A typical trajectory of a particle is also shown. The sensor consists of four parts, that is, the charged-particle rejector, the ionization surface, the wave structure in the front cylinder part, and the time-of-flight (TOF) part in the rear cylinder part. Basically all the components are symmetrical with respect to the center ($X = Y = Z = 0$).

The aperture opens on the front (right-hand side in the figure) cylinder part. The field of view is fan-shaped, which enables us to scan the whole sky by spin motion of spin-stabilized satellites, and also to scan the planetary surface by orbital motion of low-altitude three-axis-stabilized satellites.

An entering ENA through the aperture first passes through the charged-particle rejector where ambient plasmas are swept out by an electrostatic field. The charged-particle rejector also defines the geometric field of view in elevation angle by its baffle vanes and the deflection electrode.

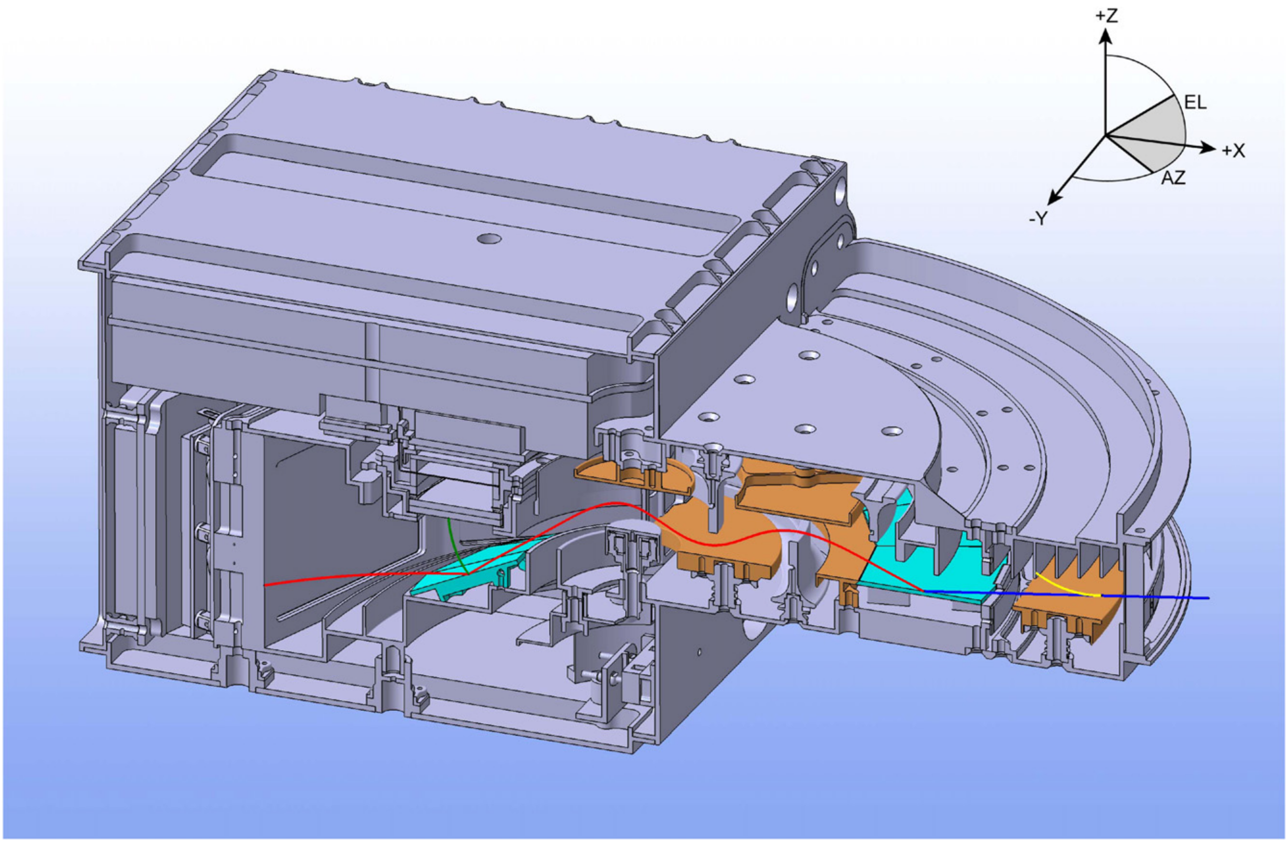

Fig. 1. Three-dimensional view of the instrument. The instrument structure is cut by the plane of $Y = 0$. The coordinate system used through this study is also shown in the figure. There is the aperture at the semicylinder part on the right side, and LENAs enter from right to left, as drawn by blue and red lines. LENAs are finally detected by detectors in the box on the left side.

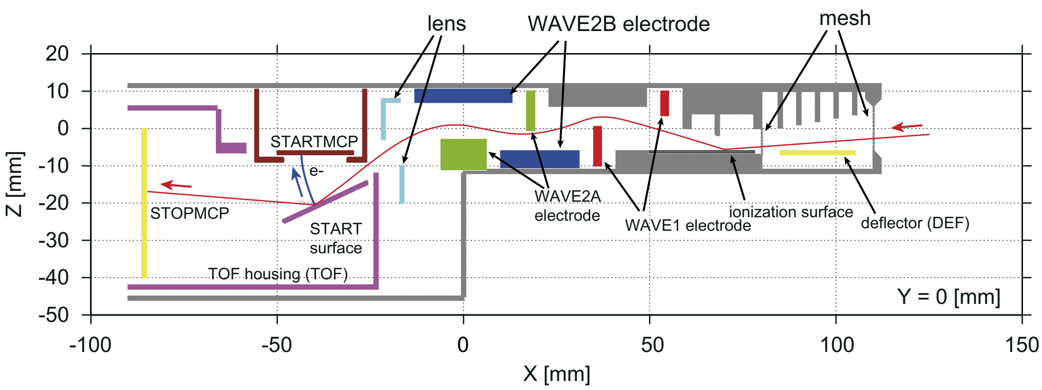

Fig. 2. Cross-sectional view of the model structure of the sensor for numerical simulations. The structure can be divided into two parts at the plane of $X = 0$. The front semicylinder part ($X > 0$) has the charged-particle rejector, the ionization surface and the wave-type structure, and the rear part ($X < 0$) has the TOF part with MCPs.

Hitting on the ionization surface, ENAs are positively ionized with a certain probability. We use tungsten-oxide surfaces as the ionization surfaces, according to studies on surface interaction of particles made in UBe. The positively ionized particle is then guided through the wave structure where the ionized particles are electrostatically guided up and down. The wave structure also makes electrostatic energy analysis, meaning that a setting of electrode voltages defines an energy range of the particles which can go through the wave structure. The upper and lower walls of the wave structure have fine serrations on their surfaces and are blackened with CuS coating to suppress photon reflection.

After the wave structure, the particles are accelerated by the lens electrodes to hit on the START surface in the TOF part. Collision of a particle with the START surface creates secondary electrons, which produce a start signal at the START MCP (micro-channel plate) for a TOF measurement. The material of the surface is tantalum in the viewpoints of less scattering effect and higher efficiency of secondary electron creation.

The particles are scattered after hitting the surface, and are finally detected by the STOP MCP to generate stop signals. By measuring a TOF between the start and stop signals, the velocity of the particle is acquired.

For the precise determination of a TOF path length, we have introduced an electron mapping method to acquire a position where the secondary electron is created. The electric field between the START surfaces and the START MCP collects electrons with the position information kept, and multiple anodes on the START MCP detect the position of origin of the electrons. We have introduced four ring anodes and seven sector anodes on the START MCP, and eight rectangular anodes on the STOP MCPs (two for each STOP MCP). The ring, sector, and rectangular anodes are referred to as 'ring', 'sector', and 'plate' anodes, respectively, hereafter for convenience. The anode positions are indicated in Fig. 3.

The seven sector anodes are placed on the backside of the START MCP at every 21.5° to cover ±75.25°, and each of them corresponds to an azimuth direction of an ENA. There are four STOP MCPs, and each STOP MCP has two plate anodes. The STOP MCPs are located to cover particles coming from all the sector anodes. A ring-sector-plate combination gives its TOF path length.

4. Voltage setting

Eight electrodes exist inside the sensor; DEF (deflector), WAVE1, WAVE2A, and WAVE2B (wave structure), LENS (lens), and TOF (TOF housing), START_MCP (input surface of START MCP), and STOP_MCP (input surface of STOP MCP), from the aperture to the detector. The potential profiles versus ENA energy are summarized in Fig. 4.

A voltage of +5000 V is applied to the electrode DEF to sweep out ambient charged particles all the time the instrument is running. Ground-potential meshes are placed on the front and rear sides of the electrode to avoid leakage of the high voltage. We expect that charged particles can also be detected if the voltage is turned off.

An ENA experiences accelerations twice inside the instrument. During passing through the wave structure, the first acceleration takes place for (1) better azimuth-angle resolution especially for low-energy ENAs, and (2) wider energy passband for larger transmittance. This acceleration is made by the electrodes WAVE1, WAVE2A and WAVE2B.

The second acceleration is between the lens and the TOF part. This acceleration contributes for (1) higher efficiency of secondary electron creation on the START surfaces, and (2) better mass resolution for low-energy ENAs by equalizing initial energies at the TOF part.

The TOF housing and the START surfaces are to have the same negative voltage (voltage of the TOF electrode; V_{TOF}) to accelerate particles. V_{TOF} is to be determined depending on the gains of the START and STOP MCPs. The voltage V_{START_MCP} is slightly higher (a few hundred volts) than V_{TOF} to collect electrons created on the START surfaces. To repel stray electrons created inside the TOF housing, V_{STOP_MCP} is several tens volts smaller than V_{START_MCP}. In the calculations shown in this study, it is assumed that $V_{TOF} = -2800$ V, $V_{START\_MCP} = -2500$ V, and $V_{STOP\_MCP} = -2850$ V.

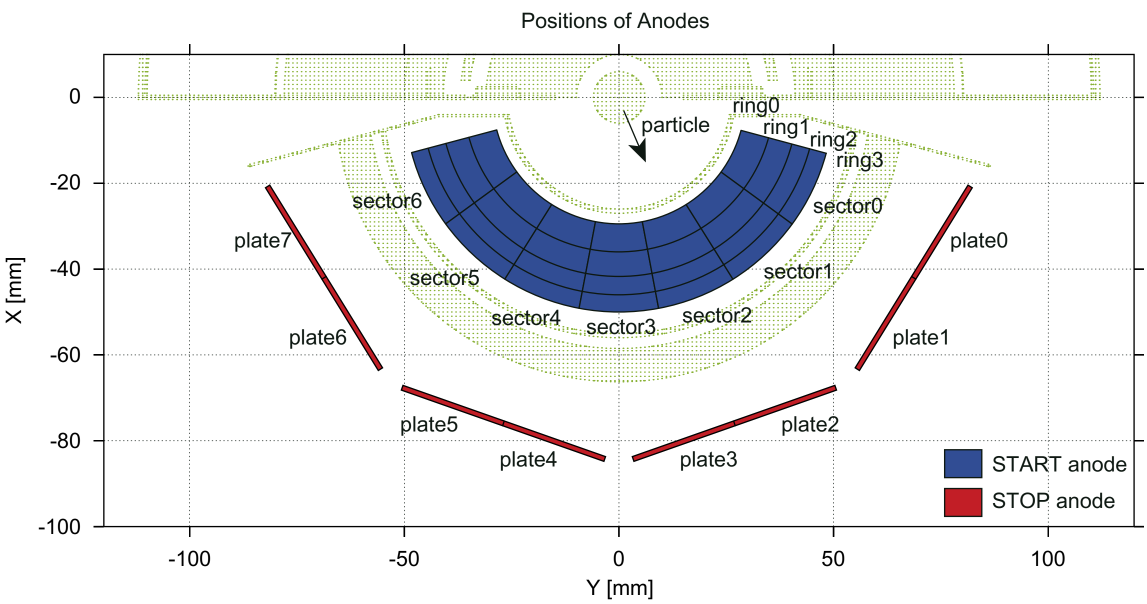

Fig. 3. Definitions of anodes on the START and STOP MCPs. The figure shows only the rear cylindrical part of the sensor. ENAs exiting from the wave structure are coming downward from the center region ($X \sim Y \sim 0$).

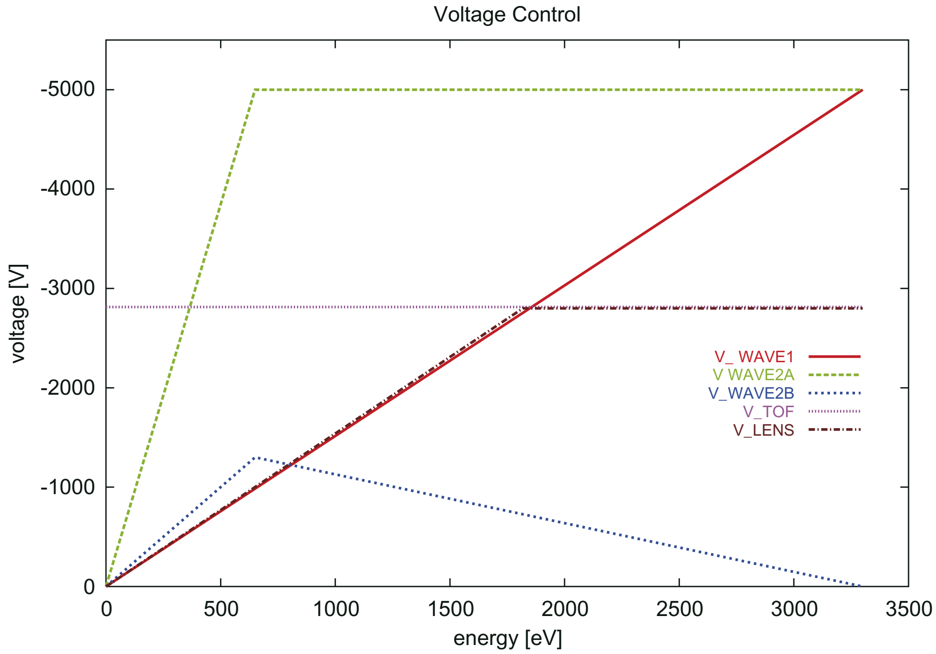

Fig. 4. Voltage profiles for each anode as a function of ENA energy. Note that the profiles shown are derived from analytical calculations and computer particle tracing.

5. Trajectory tracing code

A computer code has been newly developed for calculations of electric fields and particle trajectories. All calculations are made in three-dimensional simulation space. This code can trace trajectories of both charged and neutral particles (ions, electrons, neutral atoms, and photons).

Since the structure is expressed analytically, no approximation for a curved structure is needed. Thus, more realistic simulations, especially for photon tracing, can be done. Electric fields are calculated in regularly spaced grids by the successive over-relaxation method, and the particle tracing is made by the 4th-order Runge–Kutta method with adaptive step-size control. With particle scattering models described later, this code enables us to trace full trajectories from an aperture to a detector including particle's ionization, scattering, and secondary electron release. Instrument performances of photon rejection, ion rejection and ENA measurement were investigated, which will be shown in the following sections.

6. Performance of photon rejection

Rejection of photons is one of the crucial points of this instrument, since MCPs are sensitive to photons as well as particles. The rejection ratio of photons is obtained by a numerical photon tracing simulation. In the simulation, two types of photon reflection on a wall are assumed: (1) specular reflection with a reflection coefficient of 10^{-1} on the ionization and the START surfaces, and (2) diffuse reflection with a reflection coefficient of 10^{-2} otherwise. The walls inside the sensor are blackened with CuS, which has the coefficient of 10^{-2} for 121.6-nm light as reported by Zurbuchen et al. (1995). We assume the 10-times larger value for the ionization and the START surfaces because those surfaces are not blackened and are extremely flat.

Photons are injected randomly through the whole aperture of the sensor. The initial photon velocity in Y is always zero, meaning that the result is for the case of a Y-axis spinning satellite. A fraction of the photon decreases by reflections. For example, the initial fraction of 10^0 decreases to 10^{-2} by a diffuse reflection, and then down to 10^{-3} by a next specular reflection. This means that one tracing calculates numerous photons. The tracing stops when the fraction of the photon reaches 10^{-10}.

The 5×10^7 photons were injected in the simulation. The calculation results indicate the photon rejection ratios for the START MCP, the STOP MCP and the start surface are $r_{\mathrm{STA\_MCP}} = 4.32 \times 10^{-15}$, $r_{\mathrm{STO\_MCP}} = 2.20 \times 10^{-10}$, and $r_{\mathrm{STA\_SURF}} = 1.66 \times 10^{-12}$, respectively.

Then the photon count rates on the START MCP $c_{\mathrm{STA\_MCP}}$ and the STOP MCP $c_{\mathrm{STO\_MCP}}$ are estimated as

$$\begin{aligned} c_{\mathrm{STA\_MCP}} &= j_{\mathrm{ph}} \cdot S_{\mathrm{aperture}} \cdot \\ &\quad (r_{\mathrm{STA\_MCP}} \cdot \varepsilon_{\mathrm{ph,MCP}} + r_{\mathrm{STA\_SURF}} \cdot \varepsilon_{\mathrm{2nd,ele}} \cdot \varepsilon_{\mathrm{ele,MCP}}) \\ &= 0.4\,\mathrm{count/s}, \\ c_{\mathrm{STO\_MCP}} &= j_{\mathrm{ph}} \cdot S_{\mathrm{aperture}} \cdot r_{\mathrm{STO\_MCP}} \cdot \varepsilon_{\mathrm{ph,MCP}} \\ &= 60\,\mathrm{count/s}, \end{aligned}$$

where j_{ph} is the photon flux at a Mercury orbit, S_{aperture} is the area of the aperture, $\varepsilon_{\mathrm{ph,MCP}}$ and $\varepsilon_{\mathrm{ele,MCP}}$ are MCP's detection efficiencies for photons and electrons, respectively. These parameters are assumed as follows:

$j_{ph} = 10^{12}/\text{cm}^2\,\text{s}$, $S_{aperture} = 27\,\text{cm}^2$, $\varepsilon_{ph,MCP} = 1\%$, $\varepsilon_{2nd,ele} = 1\%$, and $\varepsilon_{ele,MCP} = 100\%$.

Finally, the coincidence count rate due to photons is calculated as

$$c_{ph,coinc} \sim c_{STA\_MCP} \cdot c_{STA\_MCP} \cdot \tau = 2 \times 10^{-5}\,\text{count/s},$$

where τ is the time window in a TOF measurement and is assumed to be 1000 ns. The count rate of ENAs is expected to be more than 0.01/s because the estimated sensitivity is more than $10^{-3}\,\text{cm}^2\,\text{sr}\,\text{eV}$ in the 25-eV case, as mentioned later. Therefore, the count rate due to photons is significantly lower than that of ENAs, indicating that photons do not affect ENA measurements.

7. Performance of ion rejection

Ambient ions must be swept out by the charged-particle rejector before reaching the ionization surfaces. Once ambient ions hit the surfaces, it is not possible to distinguish ionized neutrals from the ions. Therefore, ion rejection performance is important for ENA detection.

The rejection ratio of ions is obtained by ion tracing simulations. Here the rejection ratio is defined as the number of ions which reach the ionization surfaces to the total number of entering ions. The potential applied to the deflector is +5000 V (nominal value), and the electrodes of the wave structure are set for 25-eV ENAs.

Fig. 5 shows the profile of calculated ion transmission efficiencies. The profile is normalized to unity at infinity by fitting a function. The ratio is approximately 4×10^{-5} at 14 keV, and none of 10^6 particles reaches the surfaces at 13 keV. Therefore, the cut-off energy is between 13 and 14 keV, ~13.5 keV in conclusion.

8. Performances for ENA measurement

8.1. Calculation set-up

In this section, we show calculation results for estimating ENA measurement performances, that is, sensitivities of ENA detection, fields of view, angular resolutions, energy resolutions, and mass resolutions.

The performance is calculated in the Monte-Carlo method. Tracing a trajectory starts as a neutral particle with a randomly set initial position and velocity. Initial positions are on the sensor's aperture, and initial velocities are set widely enough to cover the whole energy passband. In tracing particles, all particle behaviors, ionization and scattering of ENAs on the ionization surface, ENA scattering and secondary electron creation on the START surfaces, are included.

When a particle reaches the ionization surface, the particle is ionized into a positive ion and is scattered according to the scattering model mentioned later. After hitting on the START surface, a secondary electron is created based on the creation model of a secondary electron (also mentioned later), and the original ion is scattered with that scattering model again. The tracing then continues for three types of particles, the secondary electron, the scattered-and-neutralized and scattered-and-charged particles. Calculations are repeated until the number of particles which hit a START surface reaches 10^4.

The calculations were made for two voltage settings, for low-energy (~25 eV) ENAs and for high-energy (~3300 eV) ENAs. Fig. 6 displays a potential distribution in the 25-eV case. Note that no STOP MCPs are shown in the figure since the potential is drawn in the plane of $Y = 0$ which does not contain the STOP MCP.

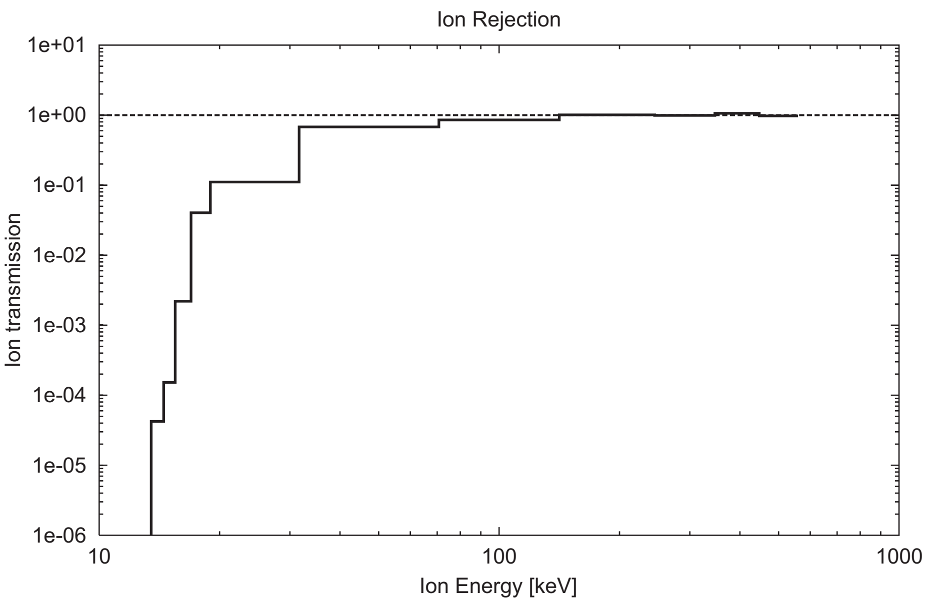

Fig. 5. Profile of ion rejection ratios versus ion energies. The profile is normalized to unity at infinity. The ratio decreases as the energy decreases, and no particle of 10^6 reaches the surface at 13 keV.

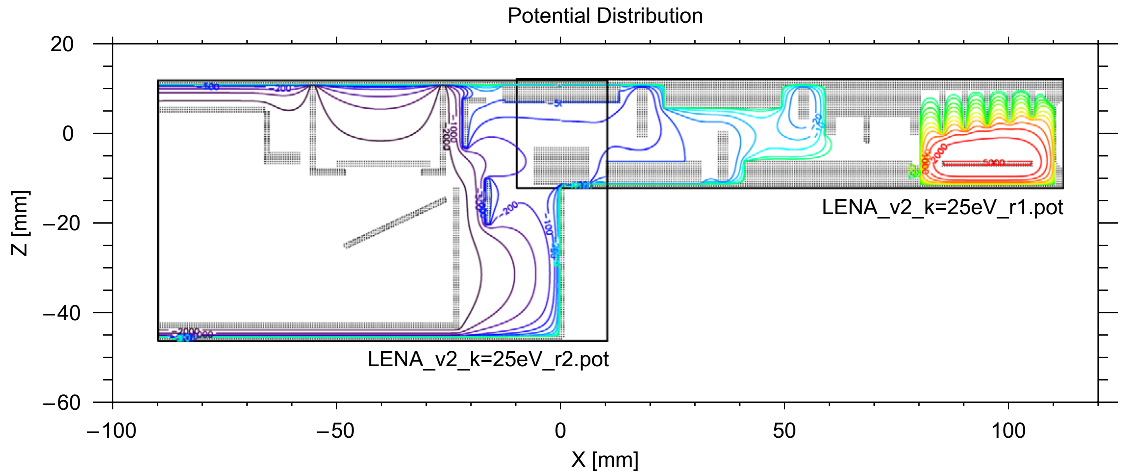

Fig. 6. Potential distribution in the case of 25-eV energy setting.

8.2. Model of particle scattering

A model of particle scattering on surfaces is used in the trajectory calculations to simulate particle scattering on the ionization and START surfaces. In this subsection, we describe the particle scattering model employed in this study.

The scattering model defines the final energy and the direction of a scattered particle. The direction of a scattered particle is defined by elevation and azimuth angles. The elevation angle is the angle of the velocity from the surface, and the azimuth angle is the direction within the surface plane. Hereafter we denote energy, elevation angle and azimuth angle by K, EL and AZ, respectively.

In the model, a final energy K_1, a final elevation angle EL_1 and a final azimuth angle AZ_1 are defined by a Gaussian distribution, which means that an average $\langle x \rangle$ and a deviation $\sigma(x)$ are needed. Accordingly, we need the profiles of $\langle K_1 \rangle$, $\sigma(K_1)$, $\langle EL_1 \rangle$, $\sigma(EL_1)$, $\langle AZ_1 \rangle$ and $\sigma(AZ_1)$.

These profiles are based on data of particle scattering experiments in literature, e.g., Wieser et al. (2002). The average and the deviation are compiled, and these discrete data points of energy, elevation and azimuth angles are fitted by analytic functions for interpolation and extrapolation, as described later.

The model is based on several assumptions:

- Scattering properties do not depend on species of incident particles.
- Ionization efficiency is constant at 10% and does not depend on the other parameters.
- Final average energies and stragglings are determined only by their initial energies.
- Elevation and azimuth angles of scattered particles are determined only by their initial elevation angles.
- Deviations of elevation and azimuth angles of scattered particles have identical properties.

In the calculation, energy loss and straggling are supposed to be proportional to initial energy; 13% and 25% of the initial energies, respectively. Therefore, the average and deviation of residual energies of scattered particles, $\langle K_1 \rangle$ and $\sigma(K_1)$ are expressed as

$$\langle K_1 \rangle = 87\% \cdot K_0,$$
$$\sigma(K_1) = 25\% \cdot K_0,$$

where K_0 means an initial energy of particles.

Averages and deviations of elevation and azimuth angles of exiting particles are defined as

$$\langle EL_1 \rangle = 0.05147(EL_0)^2 + 8.160,$$
$$\sigma(EL_1), \sigma(AZ_1) = 2.332(\sqrt{EL_0 + 1} - 1),$$

where EL_0 means initial elevation angles of incident particles. All angles are represented in degrees. These expressions are obtained by fitting data points with the functions, which do not have any scientific meaning.

8.3. Model of secondary electron creation

A secondary electron model defines an initial energy and direction of a secondary electron emitted from a surface. The model used in this study is as follows:

- Electrons are emitted uniformly in the elevation and azimuth directions, *viz.*, $EL, AZ \leftarrow$ random numbers.
- Initial energies of electrons are distributed equally from 0 to 5 eV.

In the calculations, the efficiency of secondary electron creation is assumed to be 1 (one electron, always).

8.4. Detection sensitivity

The detection sensitivity is defined as a product of a geometric factor and efficiencies. Firstly, let us think about efficiencies. The sensor has several components which reduce the number of particles to be detected; (1) transmittance of the two meshes, (2) ionization efficiency on the ionization surfaces, (3) ratio of secondary electron creation, (4) reflection efficiency on the ionization and START surfaces, and (5) detection efficiency of MCPs. These efficiencies are assumed as shown in Table 1. Therefore, the overall efficiency ε becomes $\varepsilon^2_{\text{mesh}} \cdot \varepsilon_{\text{ion}} \cdot \varepsilon_{\text{2nd,ele}} \cdot \varepsilon^2_{\text{ref}} \cdot \varepsilon_{\text{ENA,MCP}} \cdot \varepsilon_{\text{ele,MCP}} = 1.22\%$

Secondly, geometric factors are calculated by trajectory calculations with the Monte-Carlo method. Geometric factors are defined for particles which satisfy both (1) the secondary electron reaches the START MCP and (2) the particle reaches the STOP MCP.

Fig. 7 summarizes energy-integrated sensitivities including the overall efficiency of 1.22% in the low-energy (25 eV) and high-energy (3300 eV) cases. Note that since roughly 90% of particles scattered on the START surface are neutral, we neglected the ionization effect of particles scattered on the START surface for calculating the sensitivities.

According to the result, the sensitivities are of the order of 10^{-2} cm^2 sr eV for the 25-eV case, and 10^{-1} cm^2 sr eV for the 3300-eV case. The center channel (sector #3) shows a slightly smaller geometric factor because the gap between two STOP MCPs is located in the center of the channel, and some of particles are lost in the gap.

Table 1
Each efficiency of the instrument for ENA detection

	Item		Efficiency (%)
(1)	Mesh transmittance	$\varepsilon_{\text{mesh}}$	90
(2)	Ionization	ε_{ion}	10
(3)	Electron creation	$\varepsilon_{\text{2nd,ele}}$	100
(4)	Surface reflection	ε_{ref}	50
(5a)	MCP detection for ENA	$\varepsilon_{\text{ENA,MCP}}$	60
(5b)	MCP detection for electron	$\varepsilon_{\text{ele,MCP}}$	100

8.5. Angular properties

8.5.1. Definition of angles

From this section, fields-of-view (FOVs) and angular resolutions of elevation and azimuth angles are explained. Here elevation angle (EL) and azimuth angle (AZ) are defined as: $x = \cos(EL)\cos(AZ)$, $y = \cos(EL)\sin(AZ)$, $z = \sin(EL)$.

8.5.2. Elevation angle response

An elevation-angle response is displayed in Fig. 8. The result indicates the FOV of about 20° (full width), which agrees well with the range from 0° to 19.8° expected geometrically. The elevation-angle resolution is ~10° (FWHM), which is sufficient for ENA mapping measurement.

Since the FOV in elevation is defined geometrically with upper baffles and the deflection electrode at the charged-particle rejector part, the elevation-angle response does not depend on ENA energies.

8.5.3. Azimuth angle response

As mentioned previously, resolving azimuth-angle directions of ENAs is made by the sector anodes of the START MCP. Fig. 9 displays particle distributions for the sectors in the 25-eV case. The azimuth-angle resolution is roughly 25° (FWHM) at the center sector, and 30° at the side sectors (FWHM). The FOV is approximately ±75° (between the half-maximum points on the both ends).

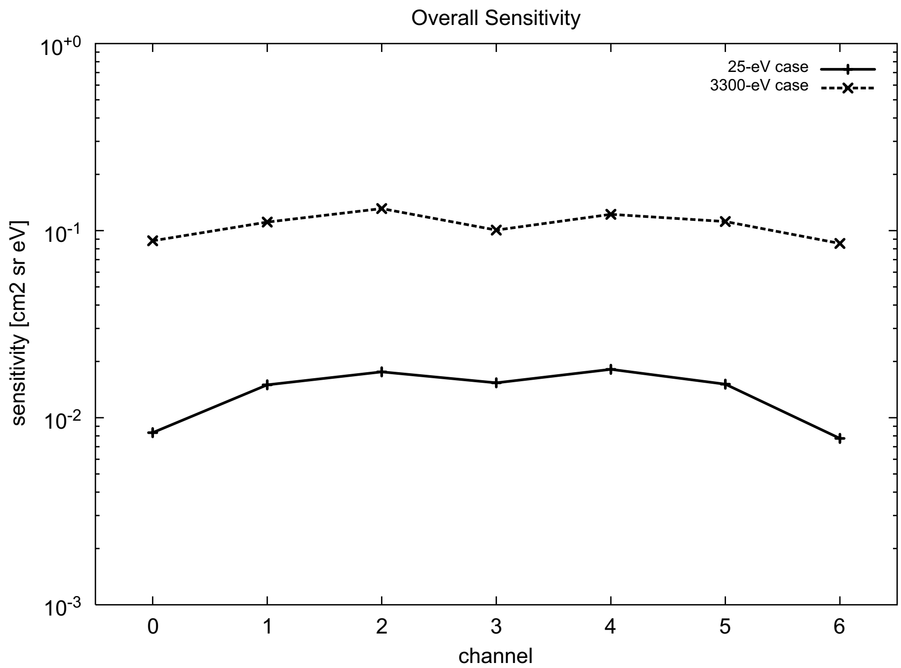

Fig. 7. Overall sensitivities for each azimuth-angle channel in the case of 25 and 3300 eV.

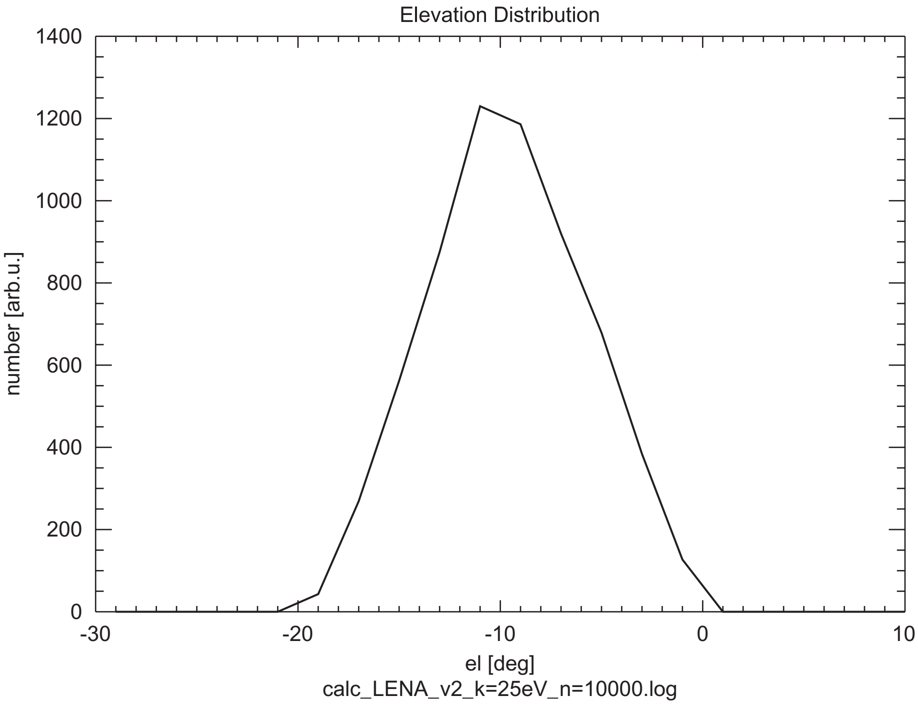

Fig. 8. Response in elevation angle in the case of the 25-eV tuning.

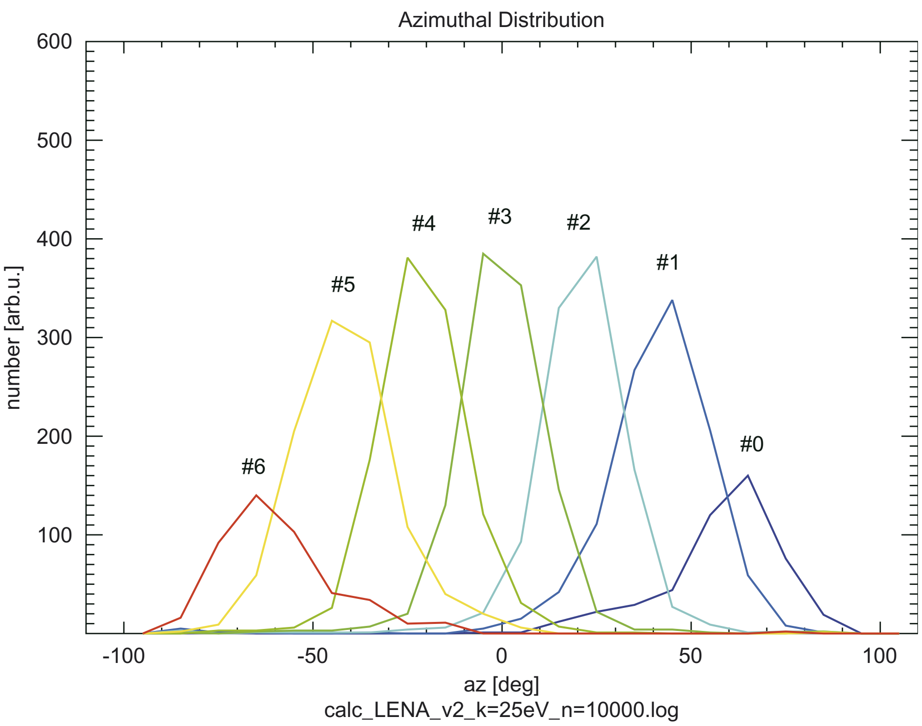

Fig. 9. Azimuth-angle response for each sector on the START MCP. The results are calculated in the potential setting for 25 eV.

This FOV agrees well with the coverage of the START-MCP anodes.

Fig. 10 shows distributions in the 3300-eV case. The resolutions are 25–30°, and the FOV is approximately ±63°, smaller than that in the 25-eV case. This is due to the distributions on the both ends. One can see that the distributions on the both ends are shifted toward the center, and those distributions are almost included in their neighboring distributions. Thus, those two sectors become less important in terms of azimuth-angle resolutions.

In order to see the cause of shifting the distributions, trajectories of some particles are displayed in Fig. 11. The figure is a top view of the sensor part with two types of trajectories of particles. One is trajectories of particles which have initial azimuth angles less than 30° and finally reach #0 sector anode (shown in blue); the other is those with initial azimuth angles greater than 65° (in red).

It is seen that the trajectories are deviated by the voltage WAVE2A of −5000 V of the inner wall electrode. The blue trajectories, which should go to #2 or #3 anode, finally reach #0 anode.

On the other hand, many of particles with large (>65°) initial azimuth angles, shown in red, are finally detected by #1, not by #0. Particles with larger azimuth angles are rarely detected due to the inner wall electrodes. This trajectory deviation is the cause of shifting the distribution.

As seen above, the electric field at the center region is sensitive to particle trajectories. Therefore, the locations and/or voltages of electrodes at the center are highly important for performances for angular resolutions and FOVs in ENA detection.

8.6. Energy response

Calculated initial energy distributions of particles are summarized in Table 2. The table shows two examples, that is, a low-energy case (25 eV) and a high-energy case (3300 eV). The peak energy (K), the energy width (ΔK) and the energy resolution ($\Delta K/K$) are given for the two energy settings. In reality, the instrument will have four energy steps to cover low- to high-energy neutral atoms.

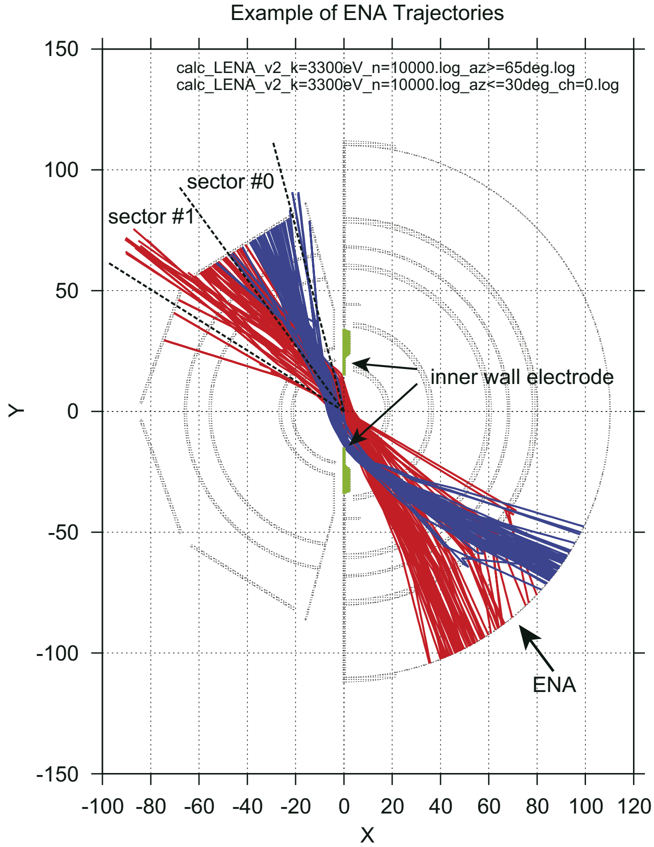

Fig. 11. Trajectories of ENAs in the top view of the sensor part. The voltages are set for 3300-eV ENAs. Two types of trajectories are plotted; blue lines are trajectories of particles which have initial azimuth angles of ⩽30° and are detected by #0 sector anode, red lines are of ⩾65° and by any sector anode.

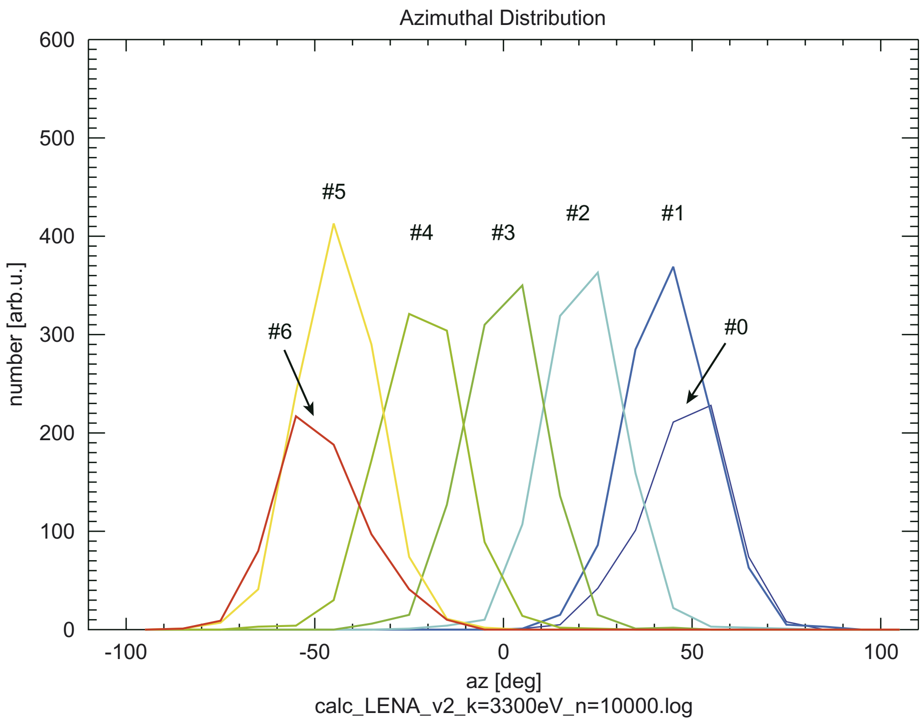

Fig. 10. Azimuth-angle response for each sector on the START MCP. The results are calculated in the potential setting for 3300 eV.

The energy resolution ranges from 70% to 107%, and decreases as the tuning energy increases. This reflects an acceleration effect which is more effective for lower-energy particles. An average energy is slightly higher than its peak value because of the tail in the higher-energy region.

8.7. Mass discrimination

A calculated TOF distribution for major species in the 25-eV case is shown in Fig. 12. The distribution was taken from the data of #3 sector anode and #4 plate anode, and the other anodes basically show same results. The figure has four TOF distributions which correspond to ring anodes #0 to #3. It is also noted that the data are for particles neutralized after START-surface scattering, and there are no differences in the results between neutralized and ionized particles.

As seen in Fig. 12, the TOF distributions range up to ~700 ns. The mass resolution is $m/\Delta m\sim 3$ or less, showing that the instrument does not distinguish between heavy species, for example, Na from Mg, K from Ca. However, information about mass groups, such as Na/Mg group and K/Ca group, can still be obtained from TOF distributions. Considering the limitations on the instrument, especially the weight limitation of 2 kg, we conclude that this mass resolution is satisfactory from the scientific point of view.

Table 2
Peak energy, energy width, and energy resolution (peak energy divided by width) are tabulated for the 25-eV and 3300-eV case

Voltage setting	Peak energy (eV)	Energy width (eV), FWHM	Resolution %
25-eV case	~28	~30	~107%
3300-eV case	~3000	~2100	~70%

Table 3
Summary of the instrument specification

Item	Figure	Unit	Remark
Weight	2	kg	Overall (sensor, electronics, etc.)
Sensitivity	$\sim 10^{-2}$	cm^2 sr eV	Per channel, for low-energy ENA
	$\sim 10^{-1}$	cm^2 sr eV	Per channel, for high-energy ENA
Energy range	~10 to >3300	eV	
Energy resolution	~70	%	For low-energy ENA
	~110	%	For high-energy ENA
Field of view	~10	°	Elevation, FWHM
	~±75	°	Azimuth, for low-energy ENA
	~±63	°	Azimuth, for high-energy ENA
Angular resolution	~10	°	Elevation, FWHM
	~25 to ~30	°	Azimuth, for low/high-energy ENA
Mass resolution	<~3		Capable of discriminating mass groups
Power consumption	~3.3	W	
Data production	2	Kbps	

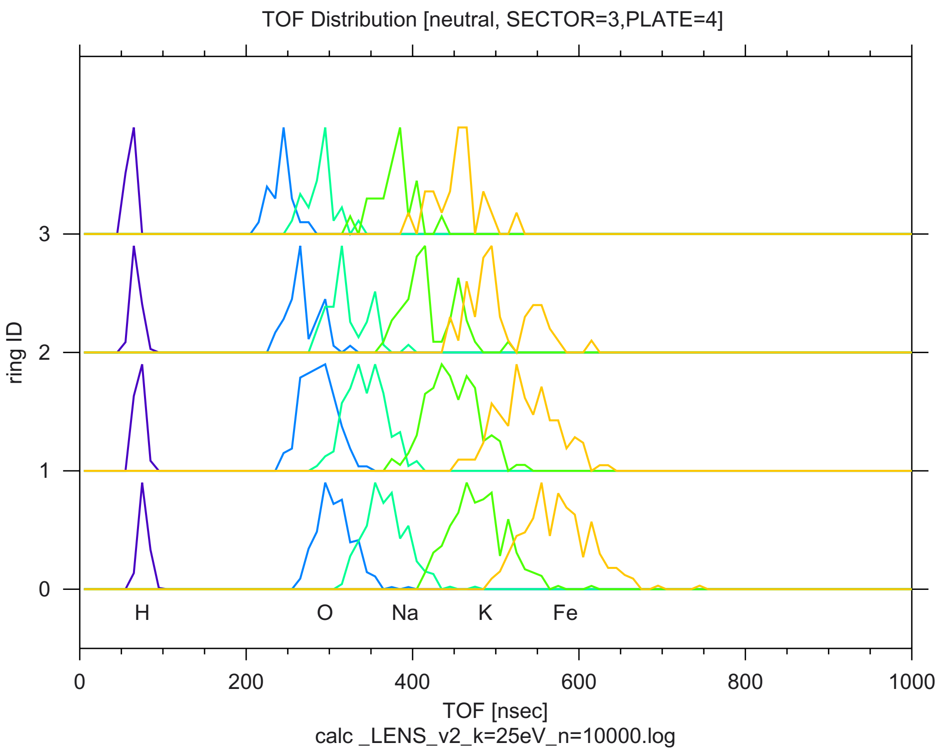

Fig. 12. TOF distributions for the ring anodes in the case of 25-eV setting. TOF data of #3 sector anode and #4 plate anode are plotted in the figure.

9. Summary

We are developing a new instrument for low-energy neutral atoms (LENAs) for planetary missions, and the performances of the instrument have been studied by computer simulations of full trajectory tracing.

The results of the simulations are summarized in Table 3. This newly developed LENA instrument covers wide energy range from ~10 to >3.3 keV to measure from ENAs sputtered from planet surfaces to those charge-exchanged or back-scattered from energetic ions. The angular resolutions are 10° in elevation and 25–30° in azimuth, and the resolutions are enough for ENA imaging observation. The instrument is capable of discriminating major mass groups of LENAs produced from the surfaces of Mercury and the Moon. This capability enables us to study sources and/or generation processes of LENAs.

Furthermore, it should be emphasized that we have achieved those performances under a 2-kg limitation of total instrument mass. To be light-weight is crucial in planetary exploration missions. This LENA instrument has been selected for both the Indian lunar exploration mission Chandrayaan-1 and European–Japanese Mercury exploration mission BepiColombo.

References

Barabash S., et al., 2004. ASPERA-3 analyser of space plasmas and energetic ions for mars express in MARS EXPRESS: the scientific payload. European Space Agency Publications Division, European Space Research & Technology Centre, Noordwijk, The Netherlands, SP-1240, pp. 121–139.

Barabash, S., et al., 2007. The analyzer of space plasmas and energetic atoms (ASPERA-4) for the Venus express mission. Planet. Space Sci., in press.

Bhardwaj, A.S., Barabash, Y., Futaana, Y., Kazama, K., Asamura, D., McCann, R., Sridharan, M., Homström, P., Wurz, Lundin, R., 2005. Low energy neutral atom imaging on the Moon with the SARA instrument aboard Chandrayaan-1 mission. J. Earth Syst. Sci. 114, 749–760.

Christon, S.P., 1987. A comparison of the Mercury and Earth magnetospheres: electron measurements and substorm time scales. Icarus, 71, 448–471.

Christon, S.P., Daly, S.F., Eraker, J.H., Perkins, M.A., Simpson, J.A., Tuzzolino, A.J., 1979. Electron calibration of instrumentation for low energy, high intensity particle measurements at Mercury. J. Geophys. Res. 84, 4277–4288.

Hovestadt, D., et al., 1995. CELIAS—charge, element and isotope analyses system for SOHO. Solar Phys. 162, 441–481.

Lin, R.P., Mitchell, D.L., Curtis, D.W., Anderson, K.A., Carlson, C.W., McFadden, J., Acuna, M.H., Hood, L.L., Binder, A., 1998. Lunar surface magnetic fields and their interaction with solar wind: results from lunar prospector. Science 281, 1480–1484.

Lukyanov, A., Barabash, S., Holmström, M., 2004. Energetic neutral atom imaging of Mercury's magnetosphere 3. Simulated images and instrument requirements. Adv. Space Res. 33, 1890–1898.

Thompson II, M.W., 1968. The energy spectrum of ejected atoms during the high energy sputtering of gold. Philos. Mag. 18, 377–414.

Wieser, M., Wurz, P., Brüning, K., Heiland, W., 2002. Scattering of atoms and molecules off a magnesium oxide surface. Nucl. Instrum. and Methods Phys. Res. B 192, 370–380.

Wurz, P., Rohner, U., Whitby, J.A., Kolb, C., Lammer, H., Dobnikar, P., Martin-Fernández, J.A., 2007. The lunar exosphere: the sputtering contribution, Icarus, submitted for publication.

Wurz, P., 2000. Detection of energetic neutral atoms the outer heliosphere: beyond the planets. In: Scherer, K., Fichtner, H., Marsch, E. (Eds.), Copernicus Gesellschaft e.V. Katlenburg-Lindau, Germany, pp. 251–288.

Zurbuchen, T., Bochsler, P., Scholze, F., 1995. Reflection of ultraviolet light at 121.6 nm from rough surfaces. Opt. Eng. 34 (5), 1303–1315.